



## Through scale material flow investigation in novel incremental bulk forming process



Joanna Szyndler<sup>a,\*</sup>, Franciszek Grosman<sup>b</sup>, Marek Tkocz<sup>b</sup>, Laurent Delannay<sup>c</sup>, Jiangting Wang<sup>d</sup>, Krzysztof Muszka<sup>a</sup>, Lukasz Madej<sup>a</sup>

<sup>a</sup> AGH University of Science and Technology, al. Mickiewicza 30, 30-059, Krakow, Poland

<sup>b</sup> Silesian University of Technology, Akademicka 2A, 44-100 Gliwice, Poland

<sup>c</sup> Université catholique de Louvain, av. Georges Lemaître, 4, B-1348 Louvain-la-Neuve, Belgium

<sup>d</sup> Institute for Frontier Materials, Deakin University, Geelong, Victoria 3217, Australia

### ARTICLE INFO

Associate Editor: Guest Editor (Exeter)

#### Keywords:

Cold forming

Multi scale modelling

Incremental bulk forming

Digital material representation

### ABSTRACT

Innovative incremental bulk forming (IBF) process dedicated to form integral elements for the aerospace industry is presented in the paper. Particular attention is put on analysis of advantages and disadvantages of this process, as well as on detailed evaluation of material flow characteristics across different length scales. Thus, a multi scale numerical model of the IBF process was established based on the isotropic hardening law at the macro scale and digital material representation concept connected with the crystal plasticity theory at the micro scale. Numerical results are also supported by a series of experimental investigations realized at the prototype of the IBF press.

### 1. Introduction

In automotive and aerospace industries, light and durable integral structures provide an opportunity to reduce CO<sub>2</sub> emission. Saha Pradip (2017) and Heinz et al. (2000) describes integral components (IC), as parts usually characterized by a complex shape, made from a single piece of material. Heinz et al. (2000) have also explained the advantages and limitations of such monolith structures with particular attention put on the production issues. In this case, the main advantage of integral parts application is the elimination of additional joining operations, which can affect part integrity. Therefore, various approaches for manufacturing of integral elements have already been established. Abele et al. (2017) analyzed a new machining process dedicated for obtaining integral titanium components applicable in the aviation and aerospace industries. They have proposed a way to improve machining based production process of IC by inductive heating and cryogenic cooling. Another possibility for the manufacturing of IC has been discussed by Yang et al. (2011). They have focused on the application of the isothermal local loading during the forming of large scale integral rib web components. Welding, brazing and extruding processes have also been investigated for the IC manufacturing by Rendigs (1997), who has focused on eliminating the conventional riveting and bonding operations in integral fuselage structures. The

integral type components could also be manufactured by a stamping process, which has been analyzed in a review paper by Merklein et al. (2014). However, from all these forming solutions for integral structures, forging seems to be a good alternative as was in detail discussed in Szyndler and Madej (2015). It is relatively fast, has good geometrical accuracy and allows controlling the final material properties what has been well presented by Zhan et al. (2014).

Unfortunately, integral elements especially for aerospace applications, are usually characterized by small thicknesses, wide surfaces and stiffening ribs. This requires large forging loads which could exceed the maximum load of conventional presses.

These issues have already been addressed in the early works of Marciniak (1970), who proposed an orbital forging concept widely used in industry. In this approach, a sample is deformed by a conical upper die, which performs incremental orbital movement, while an immobile lower die determines the final shape of the product (Fig. 1a). As a result, the load is significantly reduced in comparison to classical forging. This concept was then extended in various ways, i.e. by Shivpuri (1988), who proposed to include the orbital forging and axial die rolling processes as a subset of rotary forging.

Recently Marciniak's (1970) concept was applied to manufacture very demanding parts characterized by small thickness, wide dimensions, and essential stiffening ribs. For that Grosman et al. (2012)

\* Corresponding author.

E-mail address: [szyndler@agh.edu.pl](mailto:szyndler@agh.edu.pl) (J. Szyndler).

<https://doi.org/10.1016/j.jmatprotec.2019.116487>

Received 5 March 2019; Received in revised form 22 October 2019; Accepted 28 October 2019

Available online 16 November 2019

0924-0136/ © 2019 Elsevier B.V. All rights reserved.

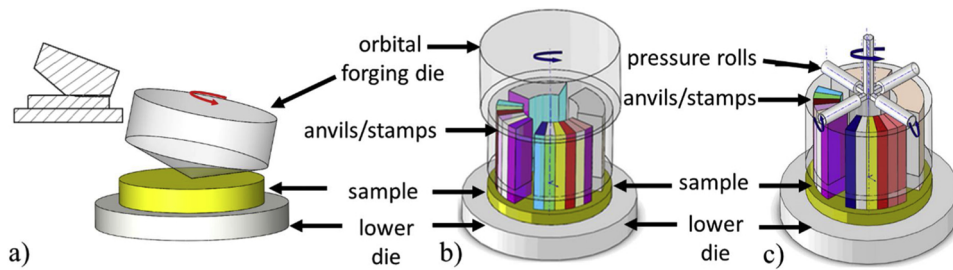


Fig. 1. Original Marciniak press concept with further modifications.

introduced an additional set of small anvils between the sample and orbiting upper die, leading to a precise division of the load into controlled small incremental deformations (Fig. 1b). To increase the incremental character of the deformation, the conical die was eventually replaced by a set of rotating rolls, transferring load to the anvils and finally to the material (Fig. 1c). However, due to the orbital/rotational movement of the upper die, only cylindrical parts could be obtained that way.

Therefore, a more general incremental bulk forming process was recently proposed by Grosman et al. (2012) and patented in Grosman et al. (2019). The concept is again based on the actuation, within a single press, of a series of small anvils, as seen in Fig. 2. Proper arrangement of anvils within sets leads to components with various shapes including e.g. stiffening ribs (Fig. 3) with very specific dimensions. In this concept, subsequent anvils are pressed into the material by the reciprocating movement of an additional die in the form of a roll. The concept can be classified as an incremental bulk cold forming (IBF) process. It is a very promising solution for manufacturing of various shapes of integral elements with small thicknesses and additional stiffening ribs. A characteristic feature of the IBF is also fibers' continuity, which strengthens the final product. Such a positive material response can be obtained only during forging and is impossible to receive by i.e. machining or casting. However, process limitations can also be identified. One of them is a problem with overflows, that may be created in the areas between anvils, due to the loss of press stiffness or tools wear. Another problem can be an occurrence of folds, that may appear when the overflows are pressed by anvils into the top surface during the process. In consequence, they may cause fractures in the surface area, increase the wear and reduce corrosion properties of the obtained product.

Therefore, to reach a proper technological readiness level of this forming technology, scientists and engineers must understand the mechanisms controlling deformation and microstructure evolution. It is not a trivial task as highly complex strain/stress states occur in the material during subsequent anvil indentations. Numerical modelling techniques can complement experimental observations which do not provide sufficient information in three dimensions.

Therefore, in this paper, the deformation mechanism and

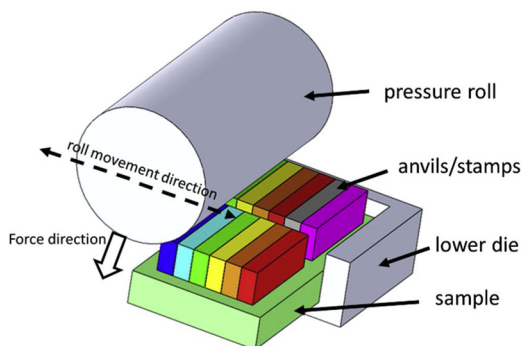


Fig. 2. IBF process concept.



Fig. 3. Sample with stiffening ribs after the IBF process.

microstructure evolution in IBF process are investigated both with experimental and numerical methods. A 2D/3D hybrid multi scale numerical model is developed to simulate material flow at different length scales; not only at the macro scale by conventional approaches, but also at the micro scale. The model adapts the Digital Material Representation (DMR) concept coupled with Crystal Plasticity (CP) theory. The model is then used to address practical questions regarding the development of the process window for this new forming technology.

## 2. Experiments

The developed prototype IBF device, which is described in detail by Szyndler et al. (2016a), was mounted within the working space of a standard hydraulic press, as seen in Fig. 4.

The case study selected for the present investigation is a setup of two sets of six anvils, moving roll and fixed lower die that enables backward extrusion for stiffening ribs creation with thickness of 5 mm (Fig. 5a). Using two sets of anvils produces a stiffening rib also in the central part of the sample. For evaluation of fundamental material behavior during the deformation, commercially pure aluminum was used as seen in Fig. 5b.

The obtained component has been subjected to detailed analysis involving macro- and microscopic metallographic investigation. First, longitudinal and perpendicular cross-section surfaces have been properly treated to reveal the underlying microstructure. Samples were ground with P800 and P1200 grade pads. Then, they were polished with diamond pastes with gradation of 9, 6, 3 and 1 μm. For the LOM (Light Optical Microscopy) analysis, samples were additionally etched with Keller's etchant for 150 s. The macro scale images of the sample cross-sections have been primarily obtained with the use of microscope as well as series of microscopic images stitched together to increase the accuracy of the investigation, as seen in Fig. 6.

As mentioned earlier, characteristic periodic continuous type fiber alignment is visible for both perpendicular and parallel directions. Additionally metal lines maintain their continuity even in the area of ribs formation where the highest deformations are observed.

Therefore, several micro scale laboratory analyses have been performed to evaluate the properties of the final product after the IBF

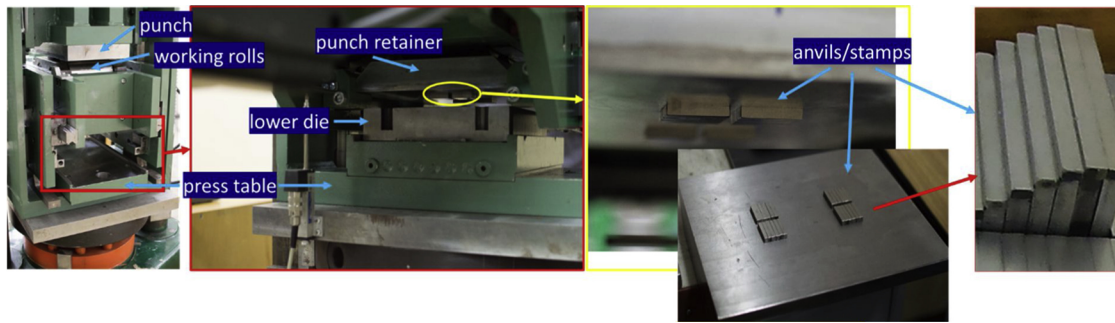


Fig. 4. Hydraulic press adapted to the IBF process.

process. First, Vickers micro-hardness map of the deformed part was obtained by Zwick/Roell ZHVµ tester (Fig. 7).

The investigated area covers the specimen under 2nd and 3rd anvil in the middle of the set. The load value was set to 100 gf. Obtained results show small variation in hardness distribution, which ranges between 35.8–38.8 HV, with no clear repetitive values alignment. In this case, sample hardness rises over 54 % during the IBF process, as the initial hardness, before deformation was 24 HV. The uniform hardness across the whole specimen thickness indicates that the IBF process imposes plastic deformation throughout the entire sample.

Electron microscopy was then used to increase the accuracy of investigation and to analyze in detail how the material behaves at the level of single grains. The SEM FEI Quanta microscope with Electron Backscatter Diffraction (EBSD) detector was used to evaluate microstructure morphology and crystallographic orientation changes. The sample was again ground with different grinding pads (240, 600, 1200 grades). This was followed by polishing operations with diamond pastes (9, 3 and 1 µm). Final polishing with colloidal silica provided high quality surface suitable to acquire EBSD maps. The SEM FEI Quanta with the TSL acquisition system was used at this stage of the investigation. This kind of imaging was realized in several interesting locations of the investigated sample, as shown in Fig. 8.

Presented results in the form of EBSD images at different locations of the sample after the incremental forming process, show various grain alignments. Grain elongation in a horizontal direction is visible in the bottom part of the sample and in the area close to the surface directly under the anvil (location no 6, 7, 8, 13, 14). In these locations under and between the anvils, grain shapes are elongated and tilted under different angles (location no 1, 2, 3, 4, 5, 9, 10, 11, 12). The area in the top part of the rib seems to be the least deformed (location no 15). The highest grain direction change is visible in the EBSD map taken from

the bottom part of the rib, close to the anvil (location no 16). Obtained results clearly show that the deformation occurs in the whole sample volume. Furthermore, high grain fragmentation takes place during the IBF process especially in the areas between the two anvils. This process is also confirmed by the high fraction of low angle grain boundaries as presented in Fig. 9.

This experimental 2D analysis has been then extended to 3D in the present paper by the development of the numerical multi scale model, to gain better insight into the presented inhomogeneities of plastic flow.

### 2.1. Development of the macro and micro models

The viscoplastic Norton-Hoff rule was used in the macro scale finite element (FE) model of the IBF process. The FE model is a fully coupled approach in the thermo-mechanical sense. The Hansel-Spittle material flow stress model, which is a function of strain, strain rate, and temperature, was used during the investigation:

$$\sigma_p = A e^{m_1 T} T^{m_9} \dot{\epsilon}_i^{m_2} e^{m_4 / \epsilon_i} (1 + \epsilon_i)^{m_5} T e^{m_7 \epsilon_i} \dot{\epsilon}_i^{m_3} \epsilon_i^{m_8} T \quad (1)$$

where:  $\sigma_p$  – flow stress;  $\epsilon_i$  – equivalent strain;  $\dot{\epsilon}_i$  – equivalent strain rate;  $T$  – temperature;  $A, m_{1-9}$  – coefficients.

To identify the model parameters, an inverse analysis method described by Szeliga et al. (2006) was selected. First, a series of uniaxial compression experiments were realized with the Gleeble 3800 thermo-mechanical simulator to provide raw data in the form of measured force-displacement curves. Samples were compressed under several combinations of strain rates (0.1, 1 and 10 s<sup>-1</sup>) and temperatures (20, 50 and 100 °C) to provide a wide range of material responses. A graphite foil was used to minimize the friction between the sample and dies.

The inverse analysis yielded the following values of coefficients in Eq. (1):  $A = 139.0, m_1 = -0.00184, m_2 = 0.0623, m_3 = 0.00933, m_4 = -$

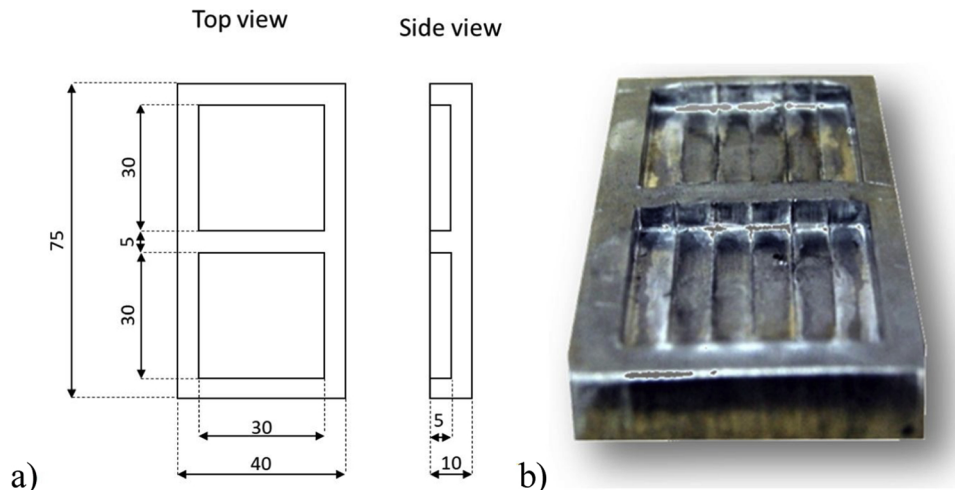


Fig. 5. Sample after the IBF process with pressing 2 sets of 6 anvils.

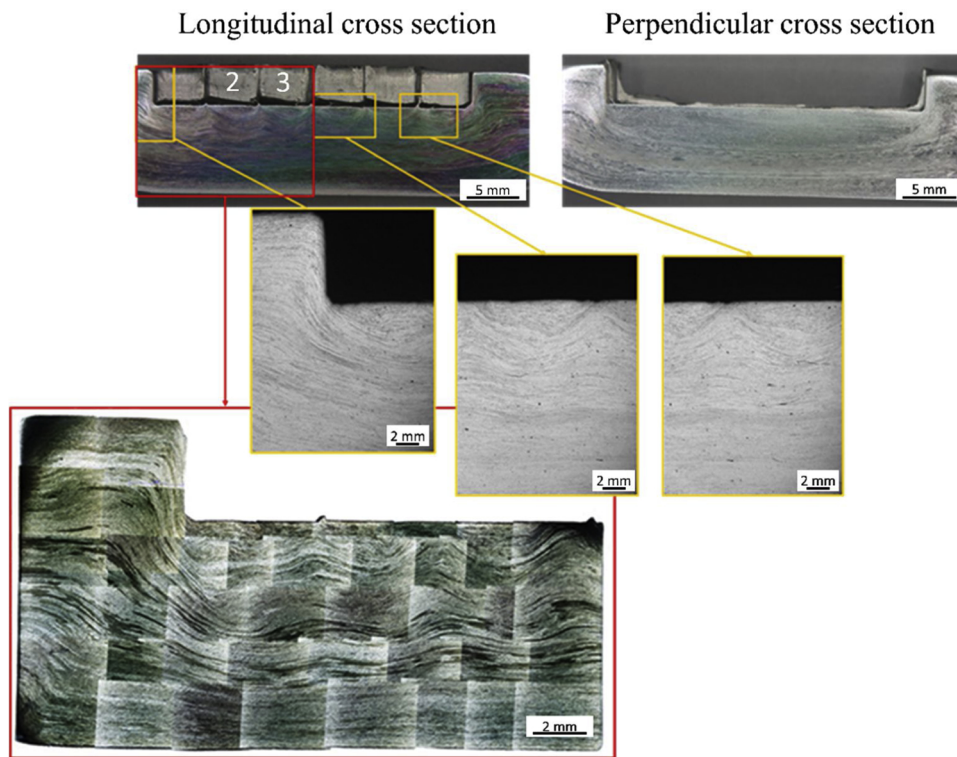


Fig. 6. State of the macro- and microstructure of the IBF sample.

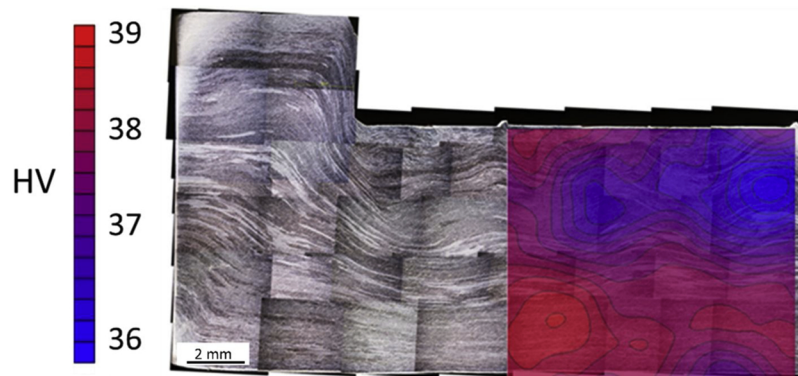


Fig. 7. Fiber alignment after IBF with Vickers micro-hardness map.

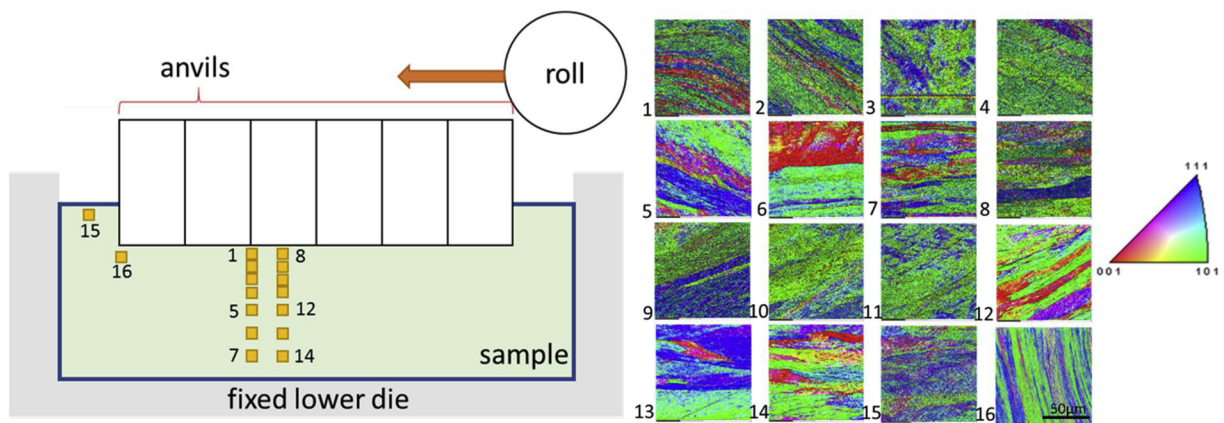


Fig. 8. Inverse pole figure-colored EBSD maps with grain boundary of the aluminum sample after the IBF process in selected sample locations.

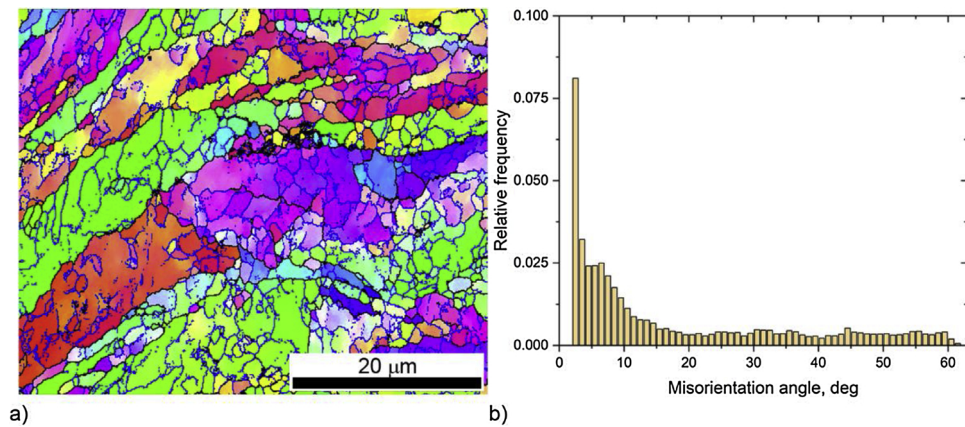


Fig. 9. a) High resolution inverse pole figure map in the area between the anvils with low (blue lines) and high (black lines) angle grain boundaries and b) corresponding grain boundaries histogram (For interpretation of the references to colour in this figure legend, the reader is referred to the web version of this article).

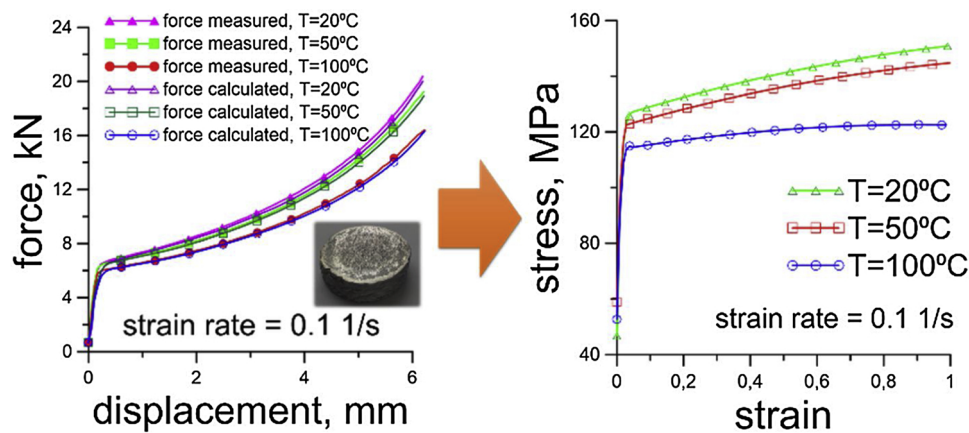


Fig. 10. Force-displacement and stress-strain curves obtained for the macro scale model after the inverse analysis.

$1.76\text{E-}05$ ,  $m_5 = -0.00186$ ,  $m_7 = 0.0631$ ,  $m_8 = 7.17\text{E-}05$ ,  $m_9 = 0.0381$ . Examples of forces recorded and calculated during the mentioned tests and stress-strain curves obtained after the inverse analysis are presented in Fig. 10.

Then, for the detailed micro scale level analysis, the digital material representation (DMR) concept was applied. Possible practical applications of the DMR concepts in the metal forming are explained in the review paper by Tekkaya et al. (2015). In that way, the DMR approach allows a description of real material morphology with different microscale features directly included (e.g. inclusions, precipitates, grains, grain boundaries, crystallographic orientations, etc.). In this case, an exact or synthetic DMR models can be generated with different numerical approaches, which are broadly discussed by Madej (2017) and then combined with the crystal plasticity (CP) model to describe local grain hardening and deformation during the IBF. In the current study, the crystal plasticity model presented by Lin et al. (2018) was used.

The DMR approach explicitly takes into account various microstructural features. The more accurate the DMR is, the more reliable results of calculations regarding material behavior are expected. EBSD was used as it provides exact information about initial grains shapes, sizes and crystallographic orientations before sample deformation. During the data acquisition process, a hexagonal scan grid with step size  $4\mu\text{m}$  was used to cover the area of approx.  $2600 \times 500\mu\text{m}$ . To maintain focus during the scan, 5 subsequent maps were acquired and then manually stitched together. The obtained EBSD images were

processed by the image analysis technique developed by Rauch and Madej (2010) in order to identify each grain as presented in Fig. 11. Due to the complexity of grain shapes, some manual corrections were also necessary.

Finally, the digital representation of the microstructure was used as input for the FE mesh generation software *DMRmesh* developed by Madej et al. (2012). The generated mesh conforms to the grain boundaries where it is selectively refined to accurately capture solution gradients.

Instead of relying on serial sectioning, which is expensive and tedious, a 3D microstructure morphology of the investigated material was generated using a modified Monte Carlo (MC) grain growth model presented by Blikstein and Tschiptschin (1999). From 2D DMR model presented in Fig. 11, the average grain size is  $225\mu\text{m}$  in the horizontal and  $138\mu\text{m}$  in the vertical direction. This was used in the MC simulations setup to generate corresponding 3D DMR morphology. Therefore, the developed DMR model (Fig. 12) is a cube with dimensions  $345 \times 345 \times 345\mu\text{m}^3$  and has 20 grains. The in-house code described in Madej et al. (2012) was used to create the finite element mesh and then flow stress data valid at micro scale was assigned to each grain using a crystal plasticity model to compute the microscopic mechanical response (Appendix A). The CP model does not take into account the influence of the temperature change, as preliminary macro scale simulations of the IBF process revealed that the temperature increase in the sample is negligible (less than  $4^\circ\text{C}$ ).

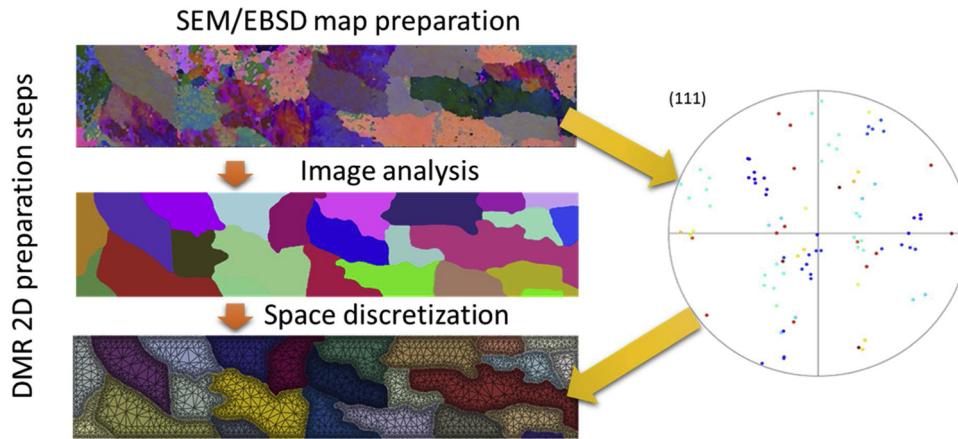


Fig. 11. DMR preparation steps in 2D spaces and the initial pole figure.

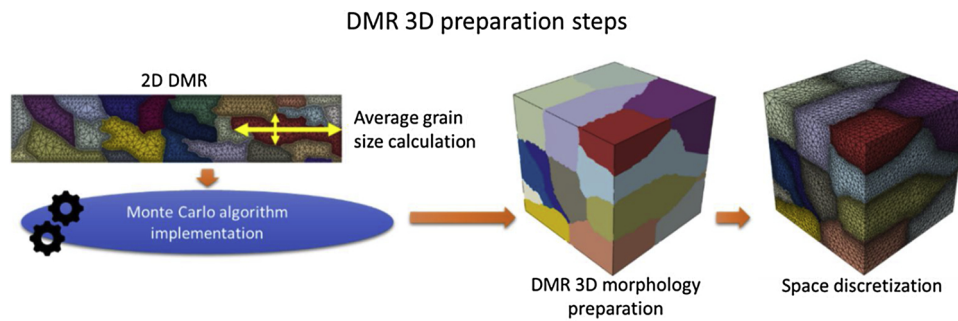


Fig. 12. DMR preparation steps in 3D space.

With the model influence of different crystallographic orientations on grain deformation could be taken into account. However, the key element influencing the accuracy of calculations is a proper identification of the coefficient of the CP equations to describe the hardening of aluminum grains with respect to their crystallographic orientations. The CP model parameters were obtained based on an inverse analysis procedure.

The experimental data to define the goal function in the mentioned inverse analysis were obtained from channel die tests of aluminum single crystals. Two mono-crystals with specific extreme crystallographic orientations were selected. Such aluminum single crystals with cube and hard initial orientations were grown by a modified Bridgman technique in the split graphite molds. Samples with dimensions of 10 mm × 10 mm × 10 mm were cut out from the obtained ingots and finally subjected to a compression test. Initial orientations of the samples are in the range of 2° of the ideal orientations. The Teflon

foil was used to minimize the influence of friction during the test. Results in the form of force-displacement curves recorded during both tests were then used as input data for the inverse analysis. During the identification, three parameters from the Swift hardening model were evaluated:  $\Gamma_0 = 0.05$ ,  $\tau_{c0} = 7$  MPa,  $n = 4$ , and obtained results are shown in Fig. 13.

As presented, the CP model accurately predicts material behavior for the two extreme conditions. However, slight overestimation in the case of cube orientation can be observed. These identified material coefficients were used in subsequent FE simulations.

Based on these models, a multi scale solution was finally established. The concept of the developed 3D multi scale model is presented in Fig. 14a. As seen, in this case, the data from the macro scale IBF model is transferred to the micro scale CP-DMR by interpolation of displacement boundary conditions (Fig. 14b).

As seen in Fig. 14b, data transfer is realized between macro and

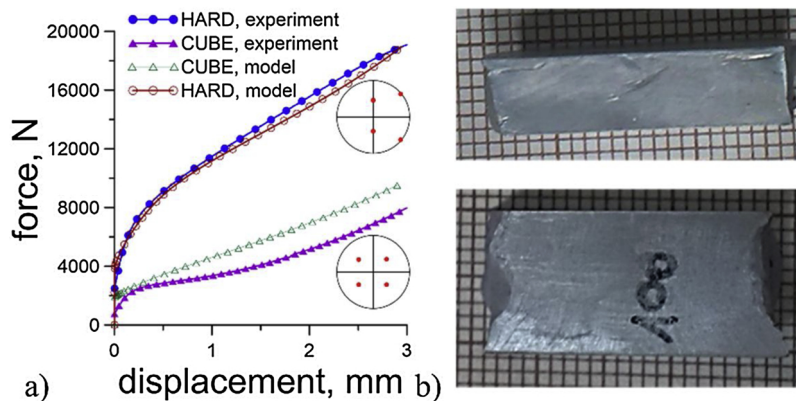


Fig. 13. a) Force-displacement curves measured and calculated after inverse analysis, b) deformed mono-crystal in cube orientation.

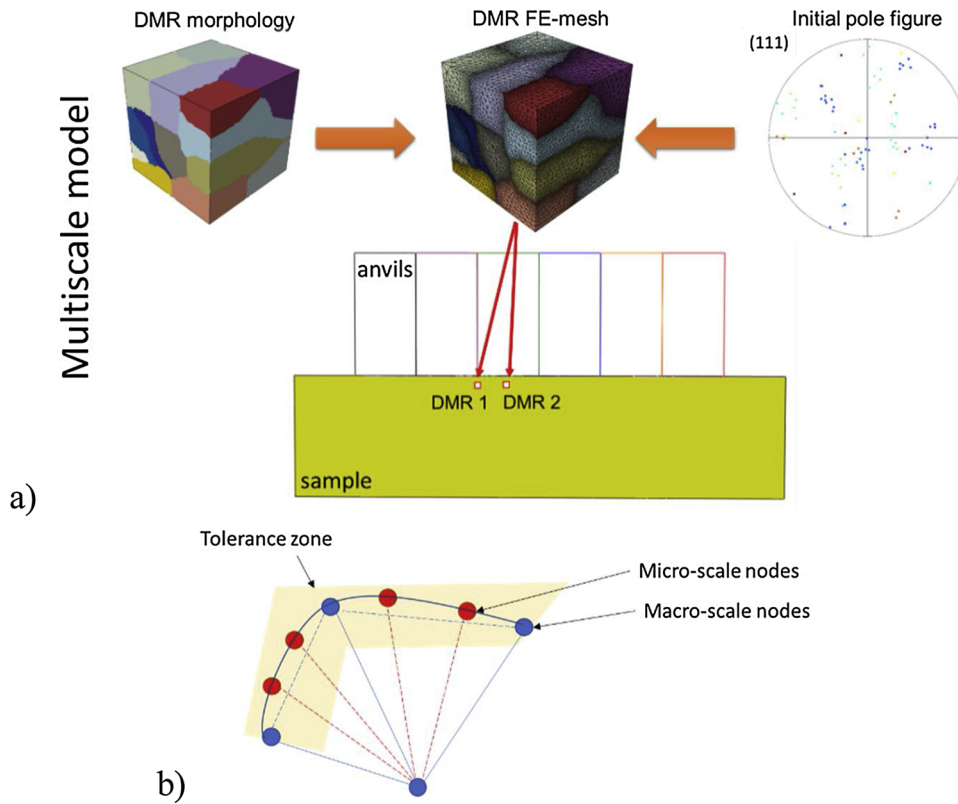


Fig. 14. a) Multi scale model and b) data transfer concept.

micro scale points which are located within the tolerance zone. As can be expected the quality of obtained results mainly depends on the number of transfer nodes at the macroscale level as coarser mesh is used in this case. The microscale model is usually discretized with very fine mesh, and a large amount of boundary nodes is available. An earlier study, presented by Szyndler et al. (2016b), on data transfer quality and its influence on obtained computational results at the micro scale provided guidelines for the present simulations of the IBF process.

### 3. Results and discussion

First, a preparatory step before IBF process modelling, was focused on the evaluation of the appropriate single anvil indentation depth under one roll pass. For this purpose, a series of calculations were realized with a simplified two dimensional FE model where a single anvil was pressed into the material up to ten different depths: 0.1, 0.2, 0.3, 0.4, 0.5, 1, 2, 3, 4 and 5 mm (Fig. 15a). Obtained results demonstrated a positive effect of dragging material on both sides of an anvil and negative effect of material bulging at the top surface (Fig. 15b).

When the indentation depth is limited, the surface of the sample is better controlled. Deeper indentations cause severe bulging of the

surface, which complicates the incremental forming process, e.g. overflows or uneven anvil wear. However, increasing the indentation depth reduces the manufacturing time. Therefore, with these criteria, it was concluded from Fig. 15b that 0.2 mm depth is the highest acceptable indentation depth. This limit value was used during both experimental and numerical analysis of material flow during the IBF process.

The IBF numerical model in general exactly replicates the setup used during the experimental investigation from chapter 2. The IBF numerical model in general exactly replicates the setup used during the experimental investigation from chapter 2. The validity of the developed macro-scale numerical model has already been proven in earlier authors' work (Szyndler et al. (2016a)).

Therefore, during current analysis, various process setups with different numbers of anvils or roll sizes have been analyzed. Performed simulations with the developed models proved the main advantage of the IBF deformation – significant load reductions. Loads recorded during the IBF were several times lower than during conventional forming, depending on the process setup (Fig. 16a). Unfortunately, it has to be also noted that, due to the cyclic character of the roll path, the energy required for the IBF deformation is higher than during conventional forming what is clearly visible in Fig. 16b. However, as

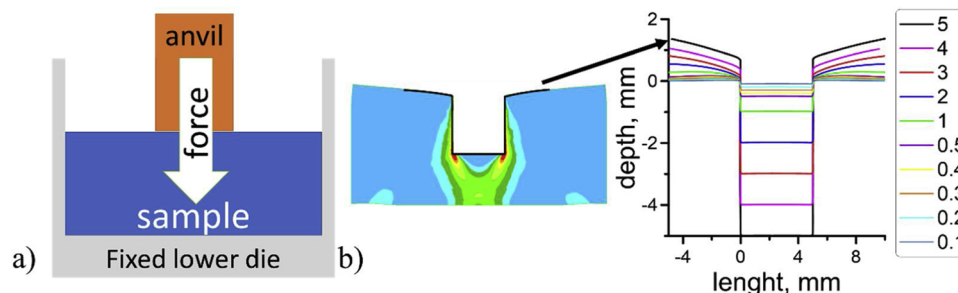


Fig. 15. a) Setup of the single anvil indentation, b) shapes of the upper part of the sample after pressing an anvil to different depths.

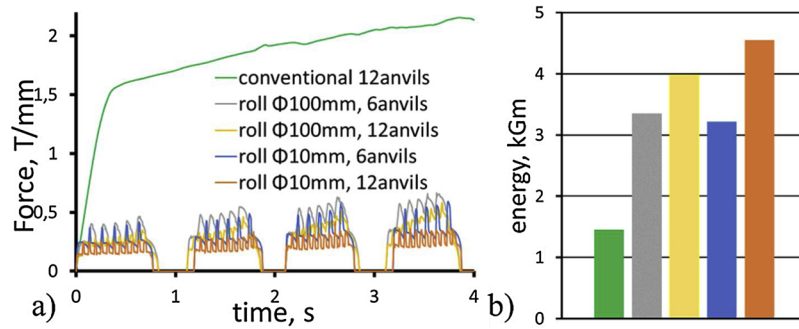


Fig. 16. a) Loads and b) corresponding energies recorded during conventional and incremental forming for various process setups.

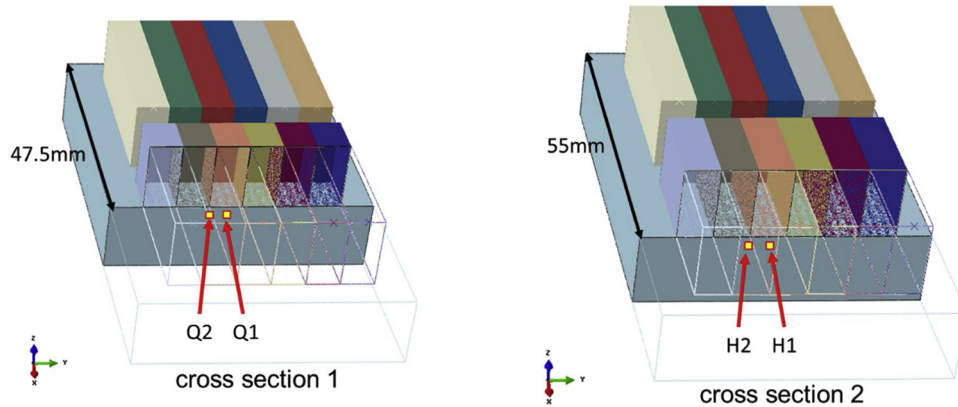


Fig. 17. The 3D multi scale model setup.

mentioned the main advantage of the IBF process is the possibility to form hardly formable materials on presses with smaller load capacities.

The next interesting issue that has to be addressed is the material behavior at the level of single grains during complex stress states in the IBF process. As mentioned, the developed 3D DMR micro model is a cube with dimensions  $345 \times 345 \times 345 \mu\text{m}^3$  and has 20 grains. All micro models have been located in the vicinity of the sample surface in four areas: underneath two anvils and directly under the center of the 3rd anvil – in half (H) and a quarter (Q) of the anvils length (Fig. 17).

This time, the simulation of four roll passes at the macro scale was performed with the roll frequency equal to 0.5 Hz and 0.2 mm indentation depth per a single roll pass to match the experimental setup. An analysis of shapes of parts obtained from the laboratory (Fig. 5) and numerical (Fig. 18) investigations show a very good correlation. Fig. 18 reveals also that the equivalent strain values especially rise along the surface and in the areas between anvils what may be associated with the strain path change effect, which is discussed in detail in the

following parts of the paper.

Grains displacement during the IBF was analyzed to investigate the influence of the third dimension on local material flow. DMR predictions of the geometry after deformation revealing changes of grains shapes are shown in Fig. 19. Also, the logarithmic strain distribution and pole figures for all calculated DMR models are shown there, to point out significant local heterogeneities.

Obtained results show that grains became elongated in the horizontal direction in locations between anvils, what is in-line with the roll movement direction and is comparable with experimental 2D results. Also, higher strain values are noticed in the areas between anvils (Q2, H2) than directly under the single anvil (Q1, H1), which also matches previous observations. Moreover, obtained pole figures clearly show that in the areas between anvils the ideal shear texture component forms during the IBF process. This leads to grain fragmentation and substructure formation similar to the Sun et al. (2011) research work, which is in line with presented earlier experimental observations.

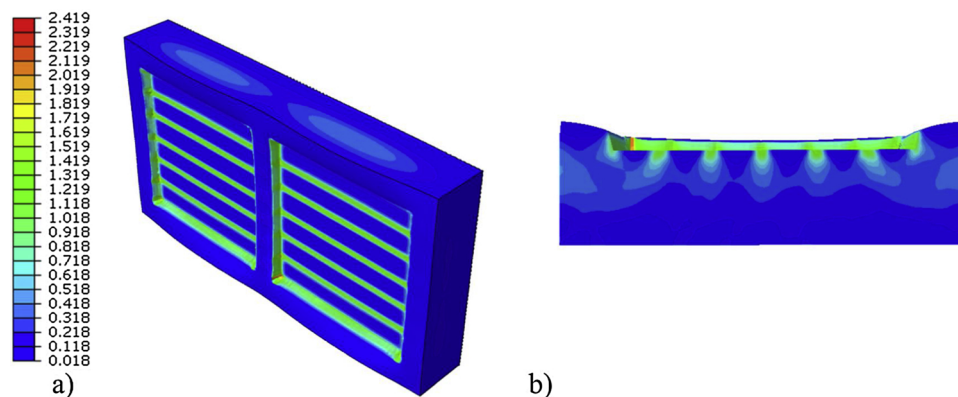


Fig. 18. Equivalent strain distribution at the macro scale after the IF process: a) overall geometry, b) cross-section in the middle of the anvils set.

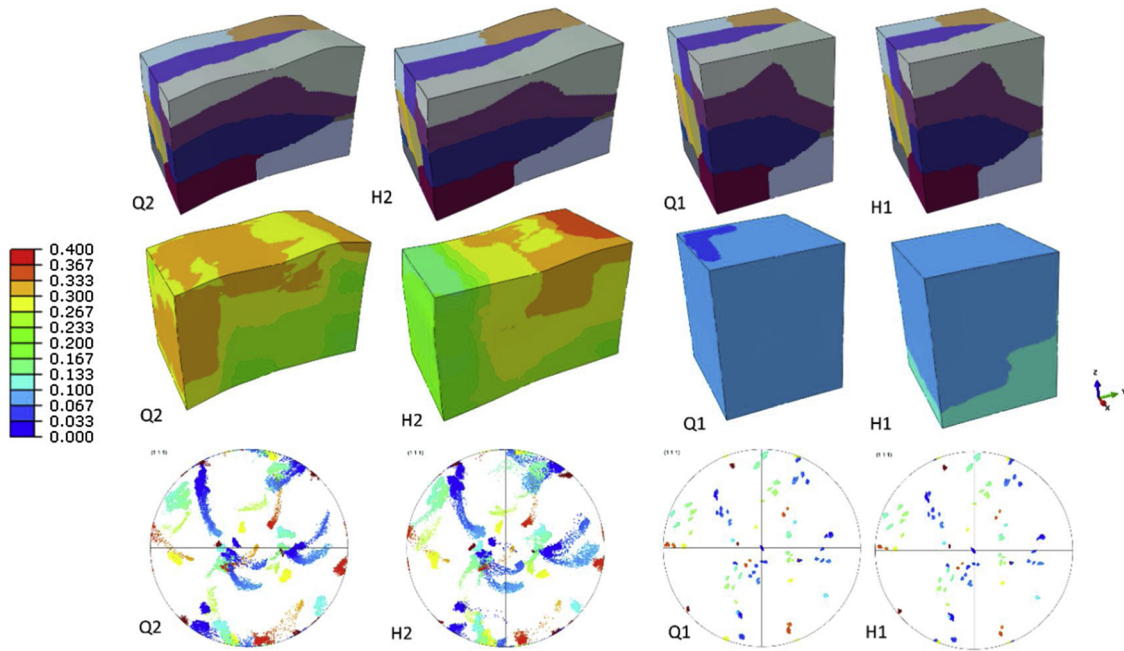


Fig. 19. Logarithmic strain distribution, grain shapes and pole figures for 3D DMR models located in the areas Q2, H2, Q1, H1.

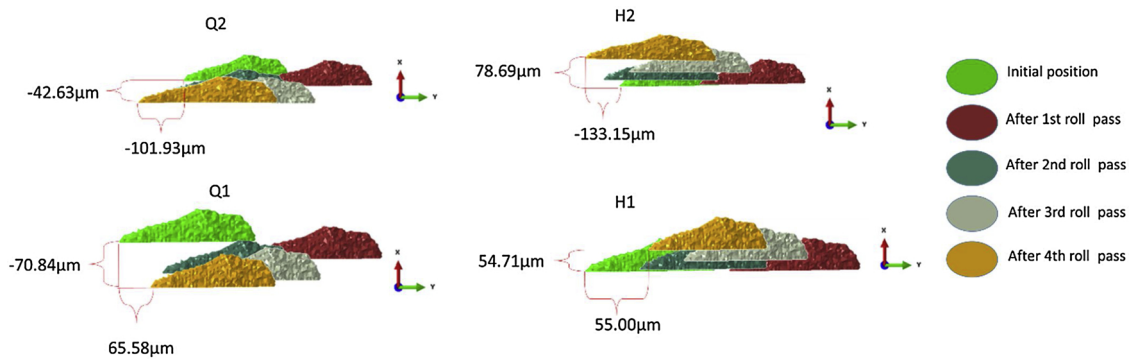


Fig. 20. Grain displacement in DMR location Q2, H2, Q1, H1.

However, this behavior is not as pronounced in locations directly under the anvils.

To investigate changes in the DMR location during the IBF along elongation and transverse directions, the position of a single grain was tracked after each roll pass, as seen in Fig. 20. Subsequent colors of grains are used in Fig. 20 to relate their position to the roll location during the IBF process. Light green is the initial/reference position of the grain before the process. Obtained results clearly show, that in all cases, there is negligible influence of the transverse direction on the obtained results. It supports the statement of generally plane strain deformation conditions in the central line of the sample.

Thus, the 2D IBF FE model can be used to analyze the influence of a large set of different process parameters without making expensive laboratory tests or running long-lasting 3D calculations.

Therefore, the faster 2D model was used in the present work to evaluate the influence of roll size (10–100 mm), movement frequency (0.1–1 Hz) and final indentation depth (0.1–0.5 mm) on material flow. Additionally, two possible ways of roll movement control were investigated. The first was based on a constant pressing depth in a single roll pass, e.g. 0.1, 0.3 or 0.5 mm (Fig. 21a). The second, on a constant velocity of roll in the vertical direction, which is related to the investigated roll frequency: 0.04, 0.2, 0.4 mm/s (Fig. 21b). Overall 378 numerical simulations have been prepared, run and analyzed to indicate the set of acceptable IBF process parameters, that maintain the

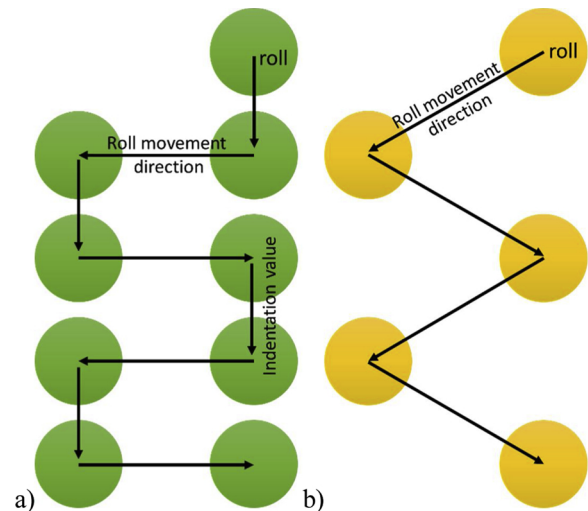


Fig. 21. Schematic illustration of roll movement direction with a) constant indentation depth, b) constant velocity during IBF process.

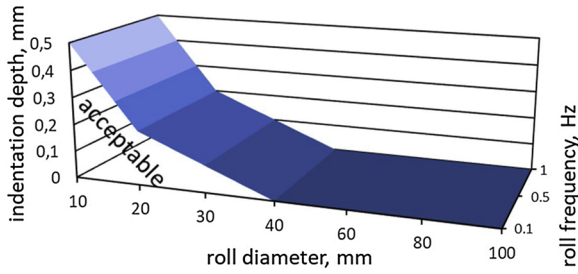


Fig. 22. Process map with acceptable process parameters combination for constant roll displacement.

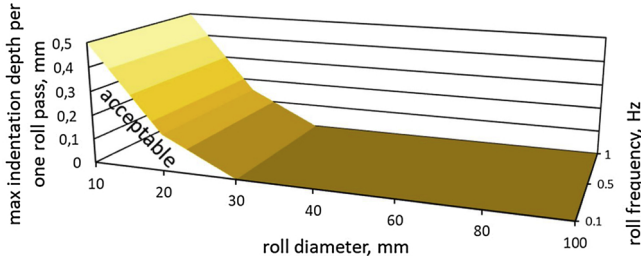


Fig. 23. Process map with acceptable process parameters combination for constant roll velocity.

incremental character of deformation (max. two anvils in contact with the roll).

The obtained results are presented in Figs. 22 and 23. Acceptable parameters, which sustain the incremental character of deformation, are gathered below the graph surface.

Given results show that the roll movement frequency has limited impact on material flow, thus required manufacturing time can be reduced. Moreover, decreasing the roll size augments the indentation depths, which additionally results in faster production. Both cases provide similar results, however the first has slightly larger process window.

Besides providing the process map, the advanced numerical model enables planning further experiments on the press prototype while lowering the risk of mistakes and problems.

## Appendix A

The general theory of crystal plasticity assumes that dislocations slip is a stress-driven phenomenon that appears along well defined crystallographic directions and planes. In the CP models elastic and plastic strains are usually distinguished, based on a multiplicative decomposition of the deformation gradient tensor:

$$\mathbf{F} = \mathbf{F}^{el} \mathbf{F}^p = \mathbf{R}^* \mathbf{U}^{el} \mathbf{F}^p \quad (1)$$

where:  $\mathbf{F}^p$  – transforms the initial configuration into an intermediate configuration that corresponds to a crystal deformed only by a dislocation slip (Fig. A1),  $\mathbf{F}^{el}$  represents the subsequent transformation that can be decomposed into a  $\mathbf{U}^{el}$ , which is a asymmetric tensor of the elastic stretch and  $\mathbf{R}^*$  that is an orthogonal tensor that represents crystal lattice rotation.

The velocity gradient  $\mathbf{L}$  is defined as:

$$\mathbf{L} = \dot{\mathbf{F}} \mathbf{F}^{-1} = \dot{\mathbf{R}}^* \mathbf{R}^{*T} + \mathbf{R}^* (\dot{\mathbf{U}}^{el} \mathbf{U}^{el-1}) \mathbf{R}^{*T} + \mathbf{R}^* \mathbf{U}^{el} (\dot{\mathbf{F}}^p \mathbf{F}^p{}^{-1}) \mathbf{U}^{el-1} \mathbf{R}^{*T} \quad (2)$$

The plastic velocity gradient is computed as the sum of shear rates on slip systems signposted with the superscript  $\alpha$  from the equation:

$$\mathbf{L}^p = \dot{\mathbf{F}}^p \mathbf{F}^p{}^{-1} = \sum_{\alpha} \mathbf{M}^{\alpha} \dot{\gamma}^{\alpha} \quad (3)$$

where:  $\mathbf{M}^{\alpha}$  – Schmid tensor that represents the dyadic product of the slip direction  $\mathbf{b}^{\alpha}$  with the normal to the slip plane  $\mathbf{n}^{\alpha}$ ,  $\dot{\gamma}^{\alpha}$  – rate of dislocation slip.

The elastic strain tensor  $\mathbf{E}$  can be calculated as:

$$\mathbf{E} = \frac{1}{2} (\mathbf{F}^{elT} \mathbf{F}^{el} - \mathbf{1}) = \frac{1}{2} (\mathbf{U}^{elT} \mathbf{U}^{el} - \mathbf{1}) \quad (4)$$

The second Piola-Kirchhoff stress  $\mathbf{T}$  is the work-conjugate measure of stress and is related with the Cauchy stress  $\boldsymbol{\sigma}$ , what is presented in:

$$\mathbf{T} = \det(\mathbf{F}^{el}) \mathbf{F}^{el-1} \boldsymbol{\sigma} \mathbf{F}^{el-T} = \det(\mathbf{U}^{el}) \mathbf{U}^{elT-1} \mathbf{R}^{*T} \boldsymbol{\sigma} \mathbf{R}^* \mathbf{U}^{el-1} \quad (5)$$

## 4. Conclusions

Numerical and experimental investigation on the IBF process lead to the following conclusions:

- Strain path changes occur in two directions during the forming process.
- Substructure creation is visible in the entire sample volume, even far from the anvils.
- Hardness distribution map indicates that material undergoes plastic deformation throughout the entire sample thickness and also suggests uniform distribution of mechanical properties in the final product.
- Influence of frequency of a roll movement on material behavior seems to be negligible.
- Decrease in the roll diameter gives access to larger indentation depths.
- Along with the load reduction, an increase in energy required for deformation is observed.

Thus, the IBF process can potentially be used for manufacturing of near-net-shape critical components with uniform properties, despite complex shapes, dedicated for aerospace applications.

## Ethical statement

The work has been prepared according to common ethical standards.

## Declaration of Competing Interest

The authors declare that they have no conflict of interest.

## Acknowledgments

Financial support from the National Science Center based on decision no DEC-2013/11/N/ST8/01207. FEM calculations were realized at the AGH ACK CYFRONET. LD is mandated by the FNRS Belgium.

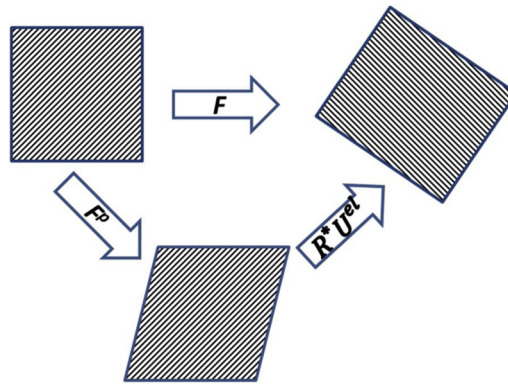


Fig. A1. Fictitious intermediate configuration used in CP modeling.

The fourth order elasticity operator  $\mathbf{c}$  sets the proportionality of  $\mathbf{T}$  with regard to  $\mathbf{E}$ :

$$\mathbf{T} = \mathbf{cE} \quad (6)$$

Finally, the theory of crystal plasticity is completed with relation between the slip rates  $\dot{\gamma}^\alpha$  and shear stress  $\mathbf{T}$ . According to the generalized Schmid law, it is assumed that slip occurs when the resolved shear stress  $\tau^\alpha$  reaches a critical value:

$$\tau^\alpha = \mathbf{T} : \mathbf{M}^\alpha \quad (7)$$

In the present work a viscoplastic expression proposed by Hutchinson (1969) and incorporated into the current CP code by Delannay et al., 2002 is used to evaluate slip rate:

$$\dot{\gamma}^\alpha = \dot{\gamma}_0 \left| \frac{\tau^\alpha}{\tau_c} \right|^{1/m} \text{sign}(\tau^\alpha) \quad (8)$$

where:  $\dot{\gamma}_0$  - reference slip rate (constant),  $m$  - sensitivity exponent (constant),  $\tau_c$  - critical resolved shear stress (CRSS) that increases due to the strain hardening.

The hardening law assumes an identical  $\tau_c$  on all slip systems, described as:

$$\tau_c = \tau_{c0} \left( 1 + \frac{\Gamma_{tot}}{\Gamma_0} \right)^n \quad (9)$$

where:  $\tau_{c0}$ ,  $\Gamma_0$ ,  $n$  - material parameters describing the evolution of the CRSS ( $\tau_c$ ) for all slip systems as a function of the accumulated plastic slip  $\Gamma_{tot}$  described by:

$$\Gamma_{tot} = \int_0^t \sum_\alpha |\dot{\gamma}^\alpha| dt \quad (10)$$

## References

- Abele, E., Hasenfratz, C., Praetzas, C., Stark, C., Kannwischer, M., Wichlas, N., 2017. Process design for rough machining of Ti6Al4V integral components. *Procedia Manuf.* 14, 118–127.
- Blikstein, P., Tschiptschin, A.P., 1999. Monte Carlo simulation of grain growth. *Mater. Res.* 2, 133–137.
- Delannay, L., Kalidindi, S.R., Van Houtte, P., 2002. Quantitative prediction of textures in aluminium cold rolled to moderate strains. *Mater. Sci. Eng. A* 336, 233–244.
- Grosman, F., Madej, L., Ziolkiewicz, S., Nowak, J., 2012. Experimental and numerical investigation on development of new incremental forming process. *J. Mater. Process. Technol.* 212, 2200–2209.
- Grosman F, Kurzydowski KJ, Pawlicki J, Tomecki L, Patent No. 210904.
- Heinz, A., Haszler, A., Keidel, C., Moldenhauer, S., Benedictus, R., Miller, W.S., 2000. Recent development in aluminium alloys for aerospace applications. *Mater. Sci. Eng. A* 280 (1), 102–107.
- Hutchinson, J.W., 1969. Creep and plasticity of hexagonal polycrystals as related to single crystal slip. *Metall. Mater. Trans. A* 8, 1465–1469.
- Lin, F., Marteleur, M., Jacques, P.J., Delannay, L., 2018. Transmission of {332}(113) twins across grain boundaries in a metastable  $\beta$ -titanium alloy. *Int. J. Plast.* 105, 195–210.
- Madej, L., 2017. Digital/virtual microstructures in application to metals engineering – a review. *Arch. Civ. Mech. Eng.* 17, 839–854.
- Madej, L., Krusel, F., Cybulka, P., Perzynski, K., Banas, K., 2012. Generation of dedicated finite element meshes for multiscale applications with delaunay triangulation and adaptive finite element – cellular automata algorithms. *Comput. Methods Mater. Sci.* 12 (2), 85–96.
- Marciniak, Z., 1970. A rocking-die technique for cold forming operations. *Mach. Prod. Eng.* 11, 792–797.
- Merklein, M., Johannes, M., Lechner, M., Kuppert, A., 2014. A review on tailored blanks – production, applications and evaluation. *J. Mater. Process. Technol.* 214 (2), 151–164.
- Rauch, L., Madej, L., 2010. Application of the automatic image processing in modelling of the deformation mechanisms based on the digital representation of microstructure. *Int. J. Multiscale Comput. Eng.* 8, 343–356.
- Rendigs, K.H., 1997. Aluminium Structures used in aerospace – status and prospects. *Mater. Sci. Forum* 242, 11–24.
- Saha Pradip, K., 2017. *Aerospace Manufacturing Processes*. CRC Press – Taylor & Francis Group.
- Shivpuri, R., 1988. Past developments and future trends in the rotary or orbital forging process. *J. Mater. Shap. Technol.* 6, 55–71.
- Sun, L., Muszka, K., Wynne, B.P., Palmiere, E.J., 2011. The effect of strain path reversal on high-angle boundary formation by grain subdivision in a model austenitic steel. *Scr. Mater.* 64, 280–283.
- Szeliga, D., Gawad, J., Pietrzyk, M., 2006. Inverse analysis for identification of rheological and friction models in metal forming. *Comput. Methods Appl. Mech. Eng.* 195, 6778–6798.
- Szyndler, J., Grosman, F., Tkocz, M., Madej, L., 2016a. Numerical and experimental investigation of the innovative incremental forming process dedicated for the aerospace industry. *Metall. Mater. Trans. A* 47, 5522–5533.
- Szyndler, J., Madej, L., 2015. Metalforming methods dedicated for aerospace industry. *Comput. Methods Mater. Sci.* 15 (2), 294–310.
- Szyndler, J., Perzynski, K., Madej, L., 2016b. Numerical analysis of data transfer quality in the 3D multi-scale uncoupled concurrent model connected with DMR. *Comput. Methods Mater. Sci.* 16, 97–103.
- Tekkaya, A.E., Allwood, J.M., Bariani, P.F., Bruschi, S., Cao, J., Gramlich, S., Groche, P., Hirt, G., Ishikawa, T., Löbbe, C., Lueg-Althoff, J., Merklein, M., Misiolek, W.Z., Pietrzyk M Shivpuri, R., Yanagimoto, J., 2015. Metal forming beyond shaping: predicting and setting product properties. *CIRP Ann. Manuf. Technol.* 64, 629–653.
- Yang, H., Fan, X.G., Sun, Z.C., Guo, L.G., Zhan, M., 2011. Some advantages in local loading precision forming of large scale integral complex components of titanium alloys. *Mater. Res. Innov.* 15 (1), 493–496.
- Zhan, M., Sun, Z., Yang, H., 2014. Modeling of hot forging. *Compr. Mater. Process.* 5,